On the nature of Pt-carbon interactions for enhanced hydrogen generation

Wenyao Chen,[a,†] Shuangming Chen,[b,†] Gang Qian,[a] Li Song,[b,*] De Chen,[c] Xinggui Zhou,[a] Xuezhi Duan[a,*]

[a]*State Key Laboratory of Chemical Engineering, East China University of Science and Technology, 130 Meilong Road, Shanghai 200237, China*

[b]*National Synchrotron Radiation Laboratory, CAS Center for Excellence in Nanoscience, University of Science and Technology of China, Hefei 230029, China*

[c]*Department of Chemical Engineering, Norwegian University of Science and Technology, N-7491 Trondheim, Norway*

Corresponding Authors: xzduan@ecust.edu.cn; song2012@ustc.edu.cn

[†]These authors contributed equally to this work.

ABSTRACT: Understanding the metal-support interactions in heterogeneous catalysis is critical yet complicated to tailor-design the catalysts with desirable properties. Exemplified with Pt-catalyzed ammonia borane (AB) hydrolysis, a dramatic increase of 20 folds in the catalytic activity is achieved by engineering the Pt-carbon interactions via adopting four different carbon materials (AC, CNT, f-CNF and p-CNF) as the catalyst supports. Multiple characterization techniques reveal that the Pt-carbon electronic interactions, including electron transfer and interfacial bonding, are deemed to be mainly responsible for the remarkable enhancement in the hydrogen generation rate. The molar ratio of electron-withdrawing group to electron-donating group (n_{EWG}/n_{EDG}) is further identified as a descriptor of catalyst in terms of Pt binding energy, which exhibits an almost linear relationship with the catalytic activity. Moreover, a comparison of Pt catalyst pre-treatments, i.e., H_2 and AB reduction as well as Ar calcination, suggests that the Pt-O-C linkages within the Pt-carbon interactions are highly stable yet inferior to this reaction. As a result, combining the merits of the highest Pt binding energy as well as the minimum Pt-O-C linkages, the Pt/p-CNF delivers the highest catalytic activity. The insights presented here could shed new lights on the nature of Pt-carbon interactions, which could be extended to the design and manipulation of other metal-carbon catalysts.

Keywords: Pt-carbon interactions; Electron transfer; Catalyst descriptor; Pt binding energy; Pt-O-C linkages.

1. Introduction

Heterogeneous catalysis has emerged as a key enabling technology in sustainable chemical processes [1-3], and the heterogeneous catalysts in practical processes generally consist of active metal (e.g., Pt, Pd, Ru, Ni, Co and Fe) and support (e.g., metal oxides and carbon) [4,5]. As a result, these supported catalysts have delivered completely different catalytic behaviors from either the metal or support. The origin of this remarkable difference has been widely recognized as the metal-support interactions, including electronic interactions (e.g., electron transfer and ligand effects) and geometric interactions (e.g., strain and relaxation) [6-8]. Hence, fundamentally understanding and further optimizing the metal-support interactions open up unprecedented opportunities to prepare highly efficient catalysts. Pioneered by Schwab, the relationships between the catalytic properties and metal-oxide interactions for different metal/oxide catalysts have been extensively studied [9-11]. For instance, a remarkable promotion in the activity and selectivity to hydrocarbon by metal oxides via the metal-oxide interactions has been demonstrated in Fischer-Tropsch synthesis over cobalt-based catalysts, which boosts extensive studies on manipulating the metal-oxide interactions for a wide range of reactions [12].

Apart from oxides, carbon materials (e.g., activated carbon, carbon nanotube, carbon nanofiber and graphene) are also frequently utilized as the catalyst support, due to their tailorable surface properties, high electron conductivity as well as easy recycling after use [13-15]. Notably, subtle variations in the catalyst preparation have been demonstrated to yield different metal-carbon interactions as well as performance

improvements by orders of magnitude [16,17]. However, to our knowledge, this metal-carbon interaction is mainly researched based on metal/graphene through theoretical calculations [18-20]. This could be due to the complex and heterogeneous surface of carbon materials, including oxygen-containing groups, surface defects and dopants, making the interpretation of theoretical results with experimental data somewhat difficult [21-23]. Therefore, an attempt is highly desirable to unravel the nature of metal-carbon interactions, thus guiding the design of metal/carbon catalysts.

From the standpoint of experiment, in order to demonstrate the metal-carbon interactions, one has to resort to the choice of proper model reaction for a proof-of-concept study. Considering the high sensitivity of carbon surface properties with temperature [24], the model reaction prefers to be conducted under ambient conditions to minimize their influences, and then correlated with the characterization results. To this point, the Pt/carbon-catalyzed ammonia borane (NH_3BH_3, AB) hydrolysis to produce hydrogen appears to be a judicious choice, which has been recognized as a highly structure-sensitive reaction under ambient conditions [25-29]. For instance, Ning et al. found that the interactions between Pt and pyridinic nitrogen (N_P) over carbon surface can promote ammonia borane hydrolysis [30]. Recently, Zhang et al. demonstrated that carbon nanotube helps stabilize highly dispersed and uniform Pt nanoparticles toward efficient hydrogen generation [31]. However, Yao et al. found that Pt nanoparticles supported on carbon black show poor catalytic activity, due to the strong adsorption affinity of hydrogen on Pt [32]. Obviously, the catalytic performances of Pt/carbon catalysts vary with the identity of carbon supports in terms of their

interactions, and a fundamental understanding of the Pt-carbon interaction would pave a way for their further design and manipulation.

In this work, we conducted a detailed and systematic study on the nature of Pt-carbon interactions and their results on catalyzing hydrogen generation from ammonia borane hydrolysis. Four types of carbon materials, i.e., activated carbon (AC), carbon nanotube (CNT), fishbone carbon nanofiber (f-CNF) and platelet carbon nanofiber (p-CNF), were adopted to prepare Pt catalysts with similar Pt particle sizes for this reaction. A combination of multiple characterizations, e.g., HAADF-STEM, N_2 physisorption, XRD, Raman, TG, H_2-TPR, XPS and XAFS, was used to probe the geometric and electronic interactions within the Pt-carbon interface, and to establish the structure-performance relationship. Moreover, different catalyst pre-treatments, including H_2 and AB reduction as well as Ar calcination, were further applied to reveal the underlying factors for fundamentally understanding the nature of Pt-carbon interactions, which would shed new lights on the design of other metal-carbon catalysts.

2. Experimental

2.1 Catalyst synthesis

Activated carbon (AC) was purchased from Sinopharm Chemical Reagent Co. Ltd. To remove the impurities on AC, it was treated with deionized water under 80 ^{o}C for 3 h. Then, the slurry was filtered and dried at 120 ^{o}C for 12 h. The multi-walled carbon nanotubes (CNT) with the purity of >98% were purchased from Beijing Cnano Technology Limited. Moreover, two types of carbon nanofibers, namely, fishbone

carbon nanofiber (f-CNF) and platelet carbon nanofiber (p-CNF), were grown in a fixed-bed quartz reactor by catalytic chemical vapor deposition (CCVD) using NiFe/γ-Al_2O_3 and Fe powders as the catalysts, respectively. Typically, these catalysts were reduced at 600 ºC for 3 h in H_2/Ar (25/75 mL·min^{-1}) followed by the growth of CNF with a mixture gas of H_2/CO (20/80 mL·min^{-1}) under the same temperature for 6 h. In order to purify the as-prepared CNF before use, they were mixed with 1 M NaOH followed by 1 M HCl aqueous solution, and each treatment lasted for 4 h at 80 ºC under vigorous agitation. The as-obtained CNF was filtered and washed by deionized water and then dried at 120 ºC for 12 h.

The different carbon supported Pt catalysts were prepared by incipient wetness impregnation method. In order to obtain the catalysts with the similar Pt particle sizes, the Pt loading was kept at 0.5 wt% for AC, while 1.5 wt% for the other three supports. Typically, the carbon support was mixed with an aqueous solution of $H_2PtCl_6{\cdot}4H_2O$ (Sinopharm Chemical Reagent Co. Ltd) and then dried in stagnant air at room temperature followed by 80 ºC for 12 h, respectively. The as-prepared Pt precursors were reduced by pure H_2 under a flow rate of 60 mL·min^{-1} at 250 ºC, and then purged with pure Ar until cooled down to room temperature. To inhibit the bulk oxidation, the reduced catalysts were exposed to 1% O_2/Ar atmosphere for 20 min to form a passivation layer [33,34], which were kept under an inert atmosphere before testing and characterizations.

2.2 Characterization

The average size and distribution of Pt nanoparticles on the carbon supports were investigated by high-angle annular dark-field scanning transmission electron microscopy (HAADF-STEM) obtained on a Tecnai G2 F20 S-Twin equipped with digitally processed STEM imaging system. The carbon supports were characterized by power X-ray diffraction (XRD) on a Rigaku D/Max2550VB/PC (Rigaku, Japan, Cu K_α radiation). The surface areas and pore volumes of carbon supports were determined by nitrogen adsorption-desorption isotherms at 77 K on a Micromeritics ASAP 2020. Before starting the adsorption measurements, all the catalysts were degassed in vacuum at 190 ºC for 6 h to remove moisture. Raman spectra were recorded on a Raman microscope (LabRAM HR, Horiba JY, France). Thermogravimetric analysis (TGA) of these carbon supports was conducted using TA SDT Q600 analyzer (TA Instruments Co., USA) under N_2 flow from room temperature to 800 ºC with a heating rate of 10 $^oC \cdot min^{-1}$. Hydrogen temperature programmed reduction (H_2-TPR) was conducted with an Autochem 2920 instrument (Micromeritics, USA) from room temperature to 900 ºC with a flow of 10% H_2/Ar (30 $mL \cdot min^{-1}$) at a heating rate of 10 $^oC \cdot min^{-1}$.

X-ray photoelectron spectroscopy (XPS) was recorded on a Kratos XSAM-800 scanning X-ray microprobe using Al K_α ($h\upsilon$=1486.6 eV) X-ray as the excitation source, and the binding energy of C 1s (284.6 eV) was utilized as the reference to correct the binding energy. Pt L_{III}-edge X-ray absorption fine structure (XAFS) of the Pt/carbon catalysts was investigated at BL14W1 beam line in the Shanghai Synchrotron Radiation Facility (SSRF) with a storage ring energy of 3.5 GeV. The X-ray was monochromatized by a double-crystal Si(311) monochromator. The energy was

calibrated using a platinum metal foil for the Pt L_3-edge. The monochromator was detuned to reject higher harmonics. Pt foil was used as a reference sample, and all samples were measured in the transmission mode, in which WinXAS3.1 code was employed to extract and fit the data [35]. Regarding the X-ray absorption near edge structure (XANES) part, the experimental absorption coefficients as a function of energies μ(E) were obtained by background subtraction and normalization procedures. The fit was made in the k-space in the range 2.8-12.7 $Å^{-1}$. Theoretical amplitudes and phase-shift functions were calculated with the FEFF8.2 code using the crystal structural parameters of the $H_2PtCl_6 \cdot 4H_2O$, PtO_2 and Pt foil [36].

2.3 Catalyst testing

The catalytic testing of hydrolytic dehydrogenation of ammonia borane (NH_3BH_3, AB, Sigma Aldrich) was carried out in a three-necked flask under atmospheric pressure. Prior to the reaction, a weighed catalyst (0.225 g for Pt/AC and 0.075 g for the other three catalysts) was preloaded into the flask. A water bath was used to control the reaction temperature at 30 ºC, and a water-filled gas burette followed by an electronic balance was connected to the reaction flask to calculate the discharged water during the reaction, which could be converted into the volume of the evolved hydrogen gas. The reaction was started by adding the aqueous ammonia borane solution (5 mL and 0.01 $g \cdot mL^{-1}$) into the flask via a syringe at the stirring speed of 900 rpm, which would help exclude the influences of mass transfer limitation [37].

3. Results and discussion

3.1 Significant carbon support effects

In order to acquire clear-cut information on the carbon supports, four types of carbon materials, i.e., AC, CNT, f-CNF and p-CNF, were adopted to prepare the similar-sized Pt catalysts by tailoring Pt loading (0.5 wt% for AC, while 1.5 wt% for CNT, f-CNF and p-CNF). To test this idea, HAADF-STEM was employed to characterize the Pt particle size and distribution of these four as-prepared catalysts, and the results are shown in Figure 1a-1d. It can be seen that the Pt nanoparticles appear as bright dots across the surfaces of AC and CNT despite of a few agglomerations. On the contrary, a uniform and homogeneous distribution of Pt nanoparticles could be observed on CNF surfaces without any significant agglomeration, especially for p-CNF. Specifically, the extremely ultrafine Pt nanoparticles in the size range of 0.8-1.3 nm are highly dispersed and densely covered on the surface of p-CNF. As a result, the Pt particle size distribution was statistically estimated based on the measurements of more than 200 random particles. As shown in the corresponding particle size histograms, both Pt/f-CNF and Pt/p-CNF exhibit narrow particle size distributions with an average diameter of 1.3±0.3 and 1.0±0.2 nm, respectively. On the contrary, Pt/AC and Pt/CNT exhibit broad particle size distributions with average diameters of 1.6±0.4 and 1.4±0.5 nm, respectively.

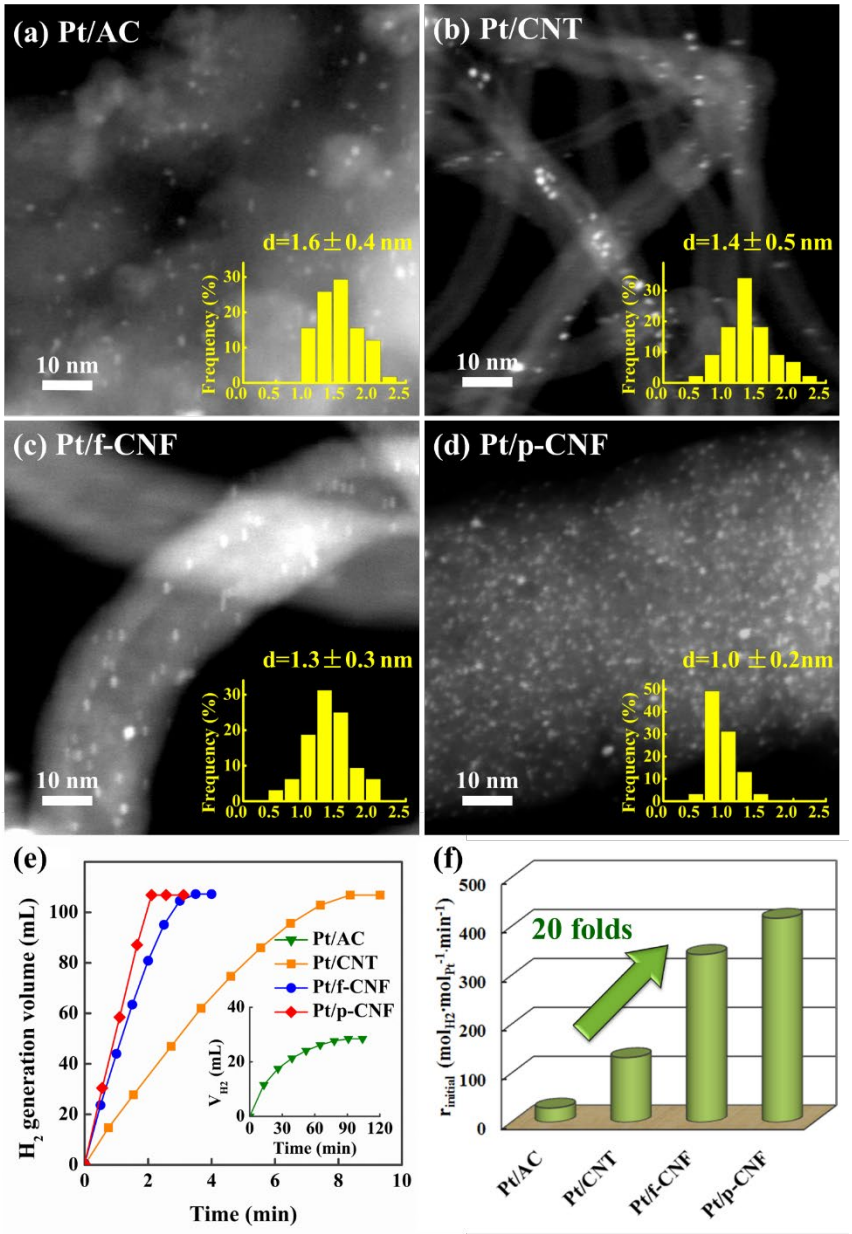

Figure 1. Typical HAADF-STEM images of (a) Pt/AC, (b) Pt/CNT, (c) Pt/f-CNF and (d) Pt/p-CNF. (e) Hydrogen generation volume as a function of time and (f) the initial reaction rate ($r_{initial}$) for Pt/AC, Pt/CNT, Pt/f-CNF and Pt/p-CNF.

To investigate the influences of the carbon supports, these four catalysts were tested for the hydrolytic dehydrogenation of ammonia borane. As shown in Figure 1e, these catalysts exhibit remarkably different catalytic behaviors, among which Pt/p-CNF delivers the highest catalytic activity and completes the reaction within 2.5 min. In

comparison, Pt/AC shows the poorest catalytic activity and less than half of generated hydrogen volume compared with the other three catalysts. All of these observations indicate strong support effects on the hydrogen generation rates for these catalysts. On the other hand, the hydrogen generation volume is found almost linearly dependent on the reaction time in the initial period (ammonia borane conversion being lower than 45±5%), indicating a zero-order reaction with respect to ammonia borane. As a result, the initial reaction rate ($r_{initial}$) could be calculated based on the slope of linear part for each plot as 21, 132, 343 and 417 $mol_{H2} \cdot mol_{Pt}^{-1} \cdot min^{-1}$ for Pt/AC, Pt/CNT, Pt/f-CNF and Pt/p-CNF, respectively. As shown in Figure 1f, a significant increase of 20 folds in the Pt catalytic activity has been achieved by varying the carbon support for the hydrolysis of ammonia borane. Moreover, previous study has suggested 1.8 nm as the optimal size of Pt nanoparticles for this reaction, below which the catalytic activity increases with Pt particle size [37]. Obviously, this trend is inconsistent with that the smallest-sized Pt/p-CNF catalyst (~1.0 nm) showing the highest catalytic activity, thus excluding Pt particle size as the main reason for the significant improvement in catalytic activity.

3.2 Structural characterization of carbon supports

To probe this support-dependent activity, nitrogen physisorption was firstly employed to characterize the textural properties of these carbon supports, and the results are summarized in Table 1. Obviously, AC involves the largest specific surface area while the smallest pore size among all the carbon supports, due to the abundant micropores within its structure. In comparison, CNT, f-CNF and p-

CNF mainly consist of mesopores as well as macropores, which facilitate the diffusion and accessibility of ammonia borane. Moreover, the observed zero-order reaction kinetics of Pt/CNT, Pt/f-CNF and Pt/p-CNF further confirm that the reaction is not limited by reactants diffusion [37]. Therefore, the mass-transfer limitations for CNT, f-CNF and p-CNF could be relieved, making them attractive as the catalyst supports for this reaction.

Table 1 Textural properties, I_{D1}/I_G, and oxygen-containing groups (OCG) content of AC, CNT, f-CNF and p-CNF.

Sample	Specific surface area ($m^2 \cdot g^{-1}$)	Pore volume ($cm^3 \cdot g^{-1}$)	Average pore diameter (nm)	I_{D1}/I_G	OCG content (wt%)
AC	952	0.47	2.0	1.49	15.3
CNT	202	1.17	13.6	1.51	3.7
f-CNF	168	0.28	65.5	1.97	5.8
p-CNF	203	0.29	51.1	2.62	5.8

Raman spectroscopy and XRD measurements were further conducted to compare their structural properties. Figure 2a displays the Raman spectra of these four supports. Two broad bands around 1347 and 1583 cm^{-1} could be observed, which correspond to the D_1 and G band, respectively. Generally, D_1 band is assigned to the disordered graphitic lattice vibration mode with A_{1g} symmetry, while G band to an ideal graphitic lattice mode with E_{2g} symmetry [38]. Thus, the intensity ratio of D_1 band to G band, I_{D1}/I_G, could be used to quantify the surface defects over the carbon supports, which is determined to be 1.49, 1.51,

1.97 and 2.62 for AC, CNT, f-CNF and p-CNF, respectively. It is obvious that the CNF supports, especially p-CNF, involve the abundant surface defects with respect to AC and CNT, which could provide more interfacial sites for the metal particles immobilization as shown in Figure 1d. As a result, p-CNF with tremendous surface defects demonstrates great potentials to prepare ultra-fine and uniformly distributed metal nanoparticles or even single-atom catalysts, which is difficult using other traditional supports. Moreover, the simultaneous presences of D_3 (~1500 cm^{-1}) and D_4 (~1200 cm^{-1}) band for AC suggest the existences of amorphous carbon and impurities, respectively [38]. Figure 2b displays the XRD patterns of these four supports, in which the strong and weak peak at 26.0° and 43.5° can be assigned to the (002) and (100) diffraction plane of hexagonal graphite, respectively. Compared with the intensive and sharp peak for CNT and CNF, the broadening of C(002) peak for AC further confirms the presence of amorphous carbon with low graphitization degree. Moreover, the absence of legible diffraction peaks ascribed to metals or their oxides for f-CNF and p-CNF indicates that the content of residual metal catalyst (Fe and Ni) for CNF growth is below XRD detection limitation after purification, which would help exclude the influence of metal impurities on the catalytic activity.

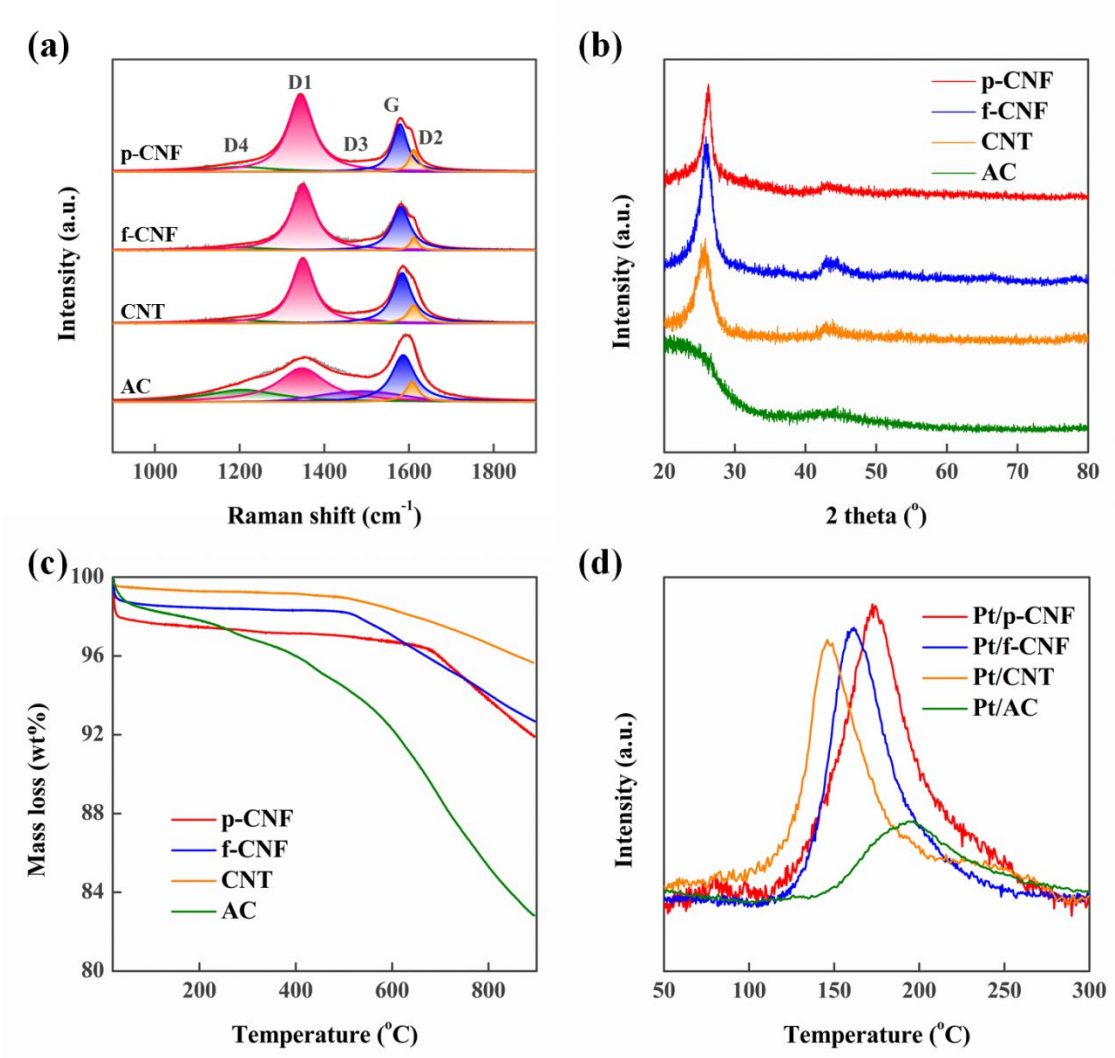

Figure 2. (a) Raman spectra, (b) XRD patterns and (c) TG profiles of AC, CNT, f-CNT and p-CNF. (d) H_2-TPR profiles of Pt/AC, Pt/CNT, Pt/f-CNF and Pt/p-CNF.

Notably, not only the surface defects but also oxygen-containing groups (OCG) over the carbon supports could affect the distribution of supported metal particles in terms of their strong interactions. Herein, the oxygen-containing groups over these carbon supports were characterized by thermogravimetric (TG) under nitrogen atmosphere (Figure 2c). In principle, the weight loss below 120 °C is mainly ascribed to the desorption of physisorbed water [39], while the remaining weight loss above 120 °C to

the decomposition of oxygen-containing groups on the carbon supports [40]. As summarized in Table 1, it is obviously that AC involves the highest amount of oxygen-containing groups (15.3 wt%), in comparison with the least of 3.7 wt% for the CNT due to its inert nature.

In addition, previous study has found that different oxygen-containing groups exhibit distinct decomposing behaviors [41]. More specifically, carboxyl and lactone groups generally begin to decompose at ca. 250 ^{o}C, while hydroxyl shows a higher decomposition temperature around 400 ^{o}C. Further increasing temperature would eliminate the residual groups such as carbonyl, anhydride and ether [41]. Based on this, AC exhibiting continuous weight loss within the whole temperature range could involve all these types of oxygen-containing groups. In contrast, CNT and f-CNF, which begin to lose weight from 500 ^{o}C, mainly involve hydroxyl, carbonyl, anhydride and ether. For p-CNF with the highest decomposition temperature around 670 ^{o}C, its surface oxygen containing group is mainly constituted by carbonyl, anhydride and ether. Based on the above analysis, it can be seen that the surface chemistry, including surface defects and oxygen-containing groups, varies significantly with the identity of carbon supports, which could give rise to different Pt-carbon interactions for catalysis.

3.3 Electron transfer within Pt-carbon interactions

To probe the interactions between the Pt nanoparticles and carbon supports, H_2 temperature programmed reduction (H_2-TPR) measurements were firstly conducted for these four catalysts. As shown in Figure 2d, the H_2-TPR profiles measured in the

temperature range from 50 to 300 ºC mainly exhibit one hydrogen consumption peak ascribed to the reduction of Pt species. It is obvious that Pt/AC and Pt/p-CNF exhibit relatively higher reduction temperatures compared with Pt/CNT and Pt/f-CNF. This could be interpreted as the presences of abundant oxygen-containing groups and surface defects for AC and p-CNF, respectively, which bind the Pt species too strongly to be reduced by H_2. Moreover, considering the lowest and highest catalytic activities for Pt/AC and Pt/p-CNF, it is reasonable to deduce that these strong Pt-carbon interactions within Pt/AC and Pt/p-CNF give rise to the inhibition and promotion effects for this reaction, respectively.

In order to bridge the different Pt-carbon interactions with their catalytic properties, X-ray photoelectron spectroscopy (XPS) was employed to characterize the electronic properties of these catalysts, and the results are shown in Figure 3. It can be seen that Pt/AC shows much weaker Pt *4f* signal compared with the other three catalysts due to its lowest Pt loading. To gain more information, the Pt 4f spectra for these catalysts were further deconvoluted into three sets of spin-orbital doublets, namely, Pt^0, Pt^{2+} and Pt^{4+} [26]. As revealed in Figure 3 and Table 2, the metallic Pt (Pt^0) emerges as the main Pt species for all the catalysts, whose binding energy follows an order of Pt/AC (71.3 eV) < Pt/CNT (71.9 eV) < Pt/f-CNF (72.0 eV) < Pt/p-CNF (72.1 eV). Considering the similarly sized Pt particles and the high electron conductivity of carbon supports, the observed binding energy shift is mainly ascribed to the electron transfer between Pt and carbon support: p-CNF captures electrons from Pt, while AC donates electrons to Pt, which give rise to the highest and lowest Pt binding energy for Pt/p-CNF and Pt/AC,

respectively.

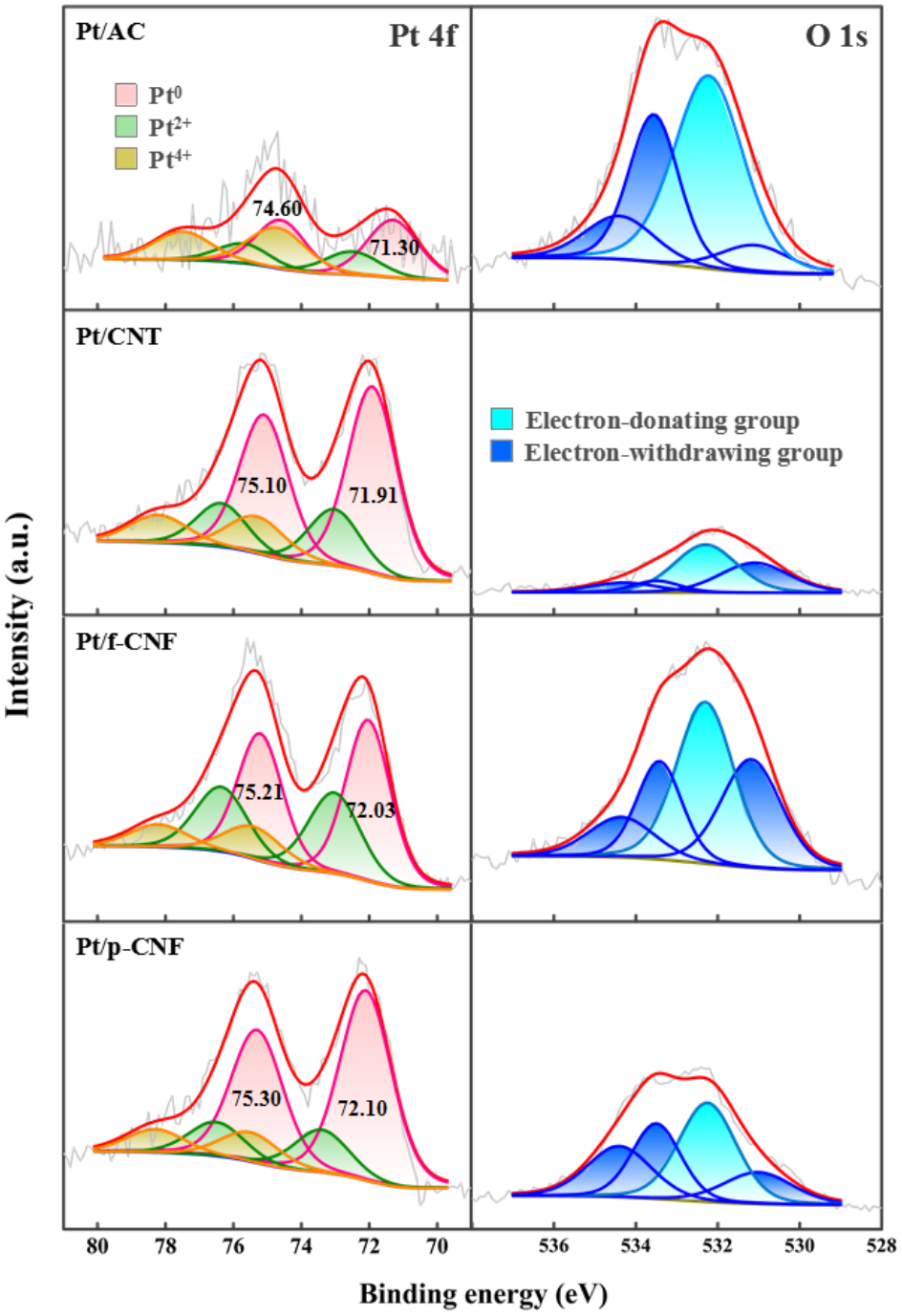

Figure 3. XPS Pt *4f* and O *1s* spectra of Pt/AC, Pt/CNT, Pt/f-CNF and Pt/p-CNF.

Table 2 The binding energy of Pt^0 $4f_{7/2}$, percentages of Pt species and O species for Pt/AC, Pt/CNT, Pt/f-CNF and Pt/p-CNF.

Catalyst	Pt^0 $4f_{7/2}$ B.E. (eV)	Pt species percentage			O species percentage			
		Pt^0	Pt^{2+}	Pt^{4+}	carbonyl	hydroxyl	anhydride, esters	carboxyl
Pt/AC	71.3	45.3%	19.3%	35.3%	7%	52%	29%	12%
Pt/CNT	71.9	64.4%	20.6%	14.9%	33%	48%	9%	10%
Pt/f-CNF	72.0	54.3%	31.6%	14.1%	27%	41%	21%	11%
Pt/p-CNF	72.1	71.0%	16.8%	12.2%	17%	37%	25%	21%

To elucidate the underlying factors of electron transfers, the O *1s* spectra for these four Pt catalysts in Figure 3 are further analyzed. Obviously, the peak intensity of O *1s* is also in accordance with the contents of oxygen-containing groups determined by TG, in which Pt/AC and Pt/CNT exhibit the strongest and weakest intensity, respectively. The O 1s spectra are further deconvoluted according to the different oxygen binding energies: C=O groups at 531.1±0.1 eV (oxygen atoms in carbonyl); O-H (oxygen atoms in hydroxyls) at 532.3±0.1 eV; ether oxygen atoms in esters and anhydrides at 533.5±0.1 eV; and oxygen atoms in carboxyl groups at 534.4±0.1 eV [42,43]. Based on this, the relative percentages of oxygen species for these catalysts are summarized in Table 2. It can be seen that hydroxyl dominates more than half of oxygen-containing groups for Pt/AC, consistent with the TG analysis on the abundance of hydroxyl over AC. Considering the electron-donating nature of hydroxyl, it could transfer electrons to the supported Pt nanoparticles, paving an explanation for the lowest Pt binding energy of Pt/AC in Figure 3. On the contrary, Pt/p-CNF mainly consists of electron-

withdrawing groups, including carbonyl, esters, anhydrides and carboxyl, and thus captures electrons from Pt particles to exhibit the highest Pt binding energy. Hence, as shown in Table 2, the competition between electron-withdrawing groups (EWG) and electron-donating groups (EDG), EWG/EDG, contributes to the gradually increased Pt binding energy for these catalysts. More interestingly, as shown in Figure 4a, it is found that the molar ratio of EWG to EDG groups, i.e., n_{EWG}/n_{EDG}, could be linearly correlated with the catalytic activity, which appears to be a good descriptor of this reaction. This can be interpreted as that the Pt surfaces become more positively charged with higher Pt binding energy, which forms stronger bonding with the negatively charged H atom in AB, that is, $Pt^{+}{-}H^{-}{-}BH_2NH_3$. As a result, it would facilitate the adsorption and activation of AB, and yield higher catalytic activity. Hence, it proves an efficient route to manipulate the types and concentrations of oxygen-containing groups, based on their electron-withdrawing/donating properties, to tailor the Pt-carbon electronic interactions in terms of the electron transfer, and thus the resultant catalytic activity.

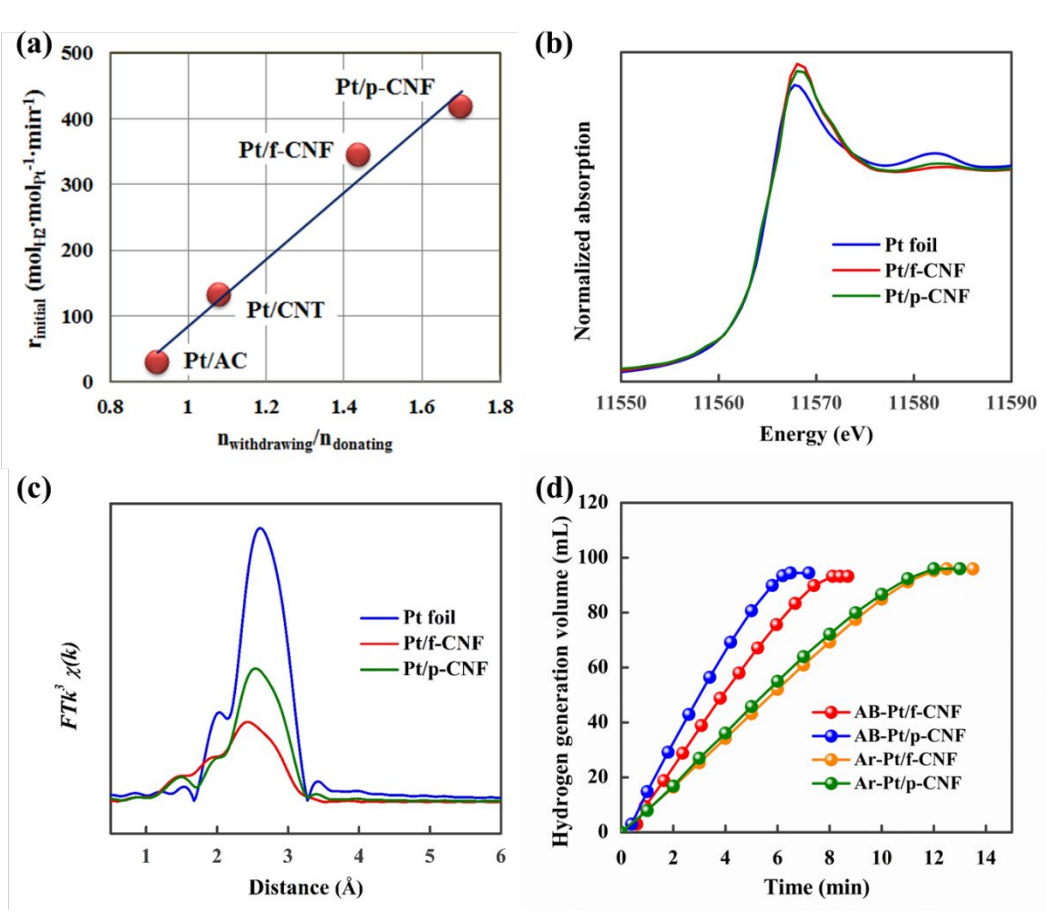

Figure 4. (a) The relationship between $r_{initial}$ and $n_{withdrawing}/n_{donating}$ for Pt/AC, Pt/CNT, Pt/f-CNF and Pt/p-CNF. (b) Normalized Pt L_{III}-edge XANES spectra, and (c) Pt L_{III}-edge k^3-weighted EXAFS spectra for Pt/f-CNF and Pt/p-CNF. (d) Hydrogen generation volume as a function of time for AB-Pt/f-CNF, AB-Pt/p-CNF, Ar-Pt/f-CNF and Ar-Pt/p-CNF.

3.4 Pt-O-C linkages within Pt-carbon interactions

Notably, as shown in Figure 3 and Table 2, not only the binding energy but also the percentage of metallic Pt^0 varies significantly for these catalysts, following an order of Pt/AC (45.3%) < Pt/f-CNF (54.3%) < Pt/CNT (64.4%) < Pt/p-CNF (71.0%). According to the catalyst preparation procedures, the presence of oxidized Pt species after H_2 reduction could originate from: (i) the Pt atoms on particle surfaces are re-oxidized in contact with air before characterizations; (ii) the Pt atoms within Pt-carbon interface

form stable species with oxygen-containing groups over the carbon surfaces despite of H_2 reduction. However, previous study has shown that a subsequent air exposure of reduced Pt catalysts for 48 h results in minimal re-oxidation [44], which indicates the unfavourable occurrence of Pt surface re-oxidation in this study. Moreover, considering that all the catalysts being passivated by 1% O_2/Ar to prohibit the bulk oxidation and then stored under an inert atmosphere before testing and characterizations, it further confirms that the Pt re-oxidation is not the main reason for the significant difference in the percentage of metallic Pt^0 [33,34]. In other words, it is more likely that some Pt atoms within Pt-carbon interfaces form strong Pt-O-C linkages with the oxygen-containing groups, especially for AC, because its surface-enriched oxygen-containing groups could strongly interact with Pt nanoparticles. Hence, not only the electron transfer (Pt binding energy) but also the interfacial bonding (Pt-O-C linkages) within the Pt-carbon interactions vary significantly with the identity of carbon support.

Herein, two typical Pt catalysts (Pt/f-CNF and Pt/p-CNF) with similar Pt binding energy were selected to study the influences of Pt-O-C linkages. Firstly, X-ray absorption fine structure (XAFS) technique, including X-ray absorption near edge structure (XANES) and extended X-ray absorption fine structure (EXAFS) spectroscopes, was employed to investigate the electronic structure and local coordination structure of Pt in these catalysts. Figure 4b displays the normalized Pt L_{III}-edge XANES profiles of these two catalysts and reference material of Pt foil. Clearly, the white-line (WL) peak around 11568 eV was identified, as a reflection of the electronic transition from $2p_{3/2}$ to unoccupied 5d states at the Pt L_{III}-edge: the high WL

intensity corresponds to higher oxidation state. Hence, Pt/f-CNF with higher WL intensity involves higher oxidation state than Pt/p-CNF. Moreover, Figure 4c displays the Fourier transformed Pt L_{III}-edge k^3-weighted EXAFS spectra, and the structural parameters obtained by the aid of EXAFS fittings are listed in Table S1. Three major contributions could be observed at the distances of ~1.85, 2.24 and 2.73 Å, originated from the shells of Pt-O, Pt-Cl and Pt-Pt, respectively. It can be seen that Pt/f-CNF exhibits decreased Pt-Pt shell fraction while increased Pt-O/Pt-Cl shell fractions compared with Pt/p-CNF. Hence, a combination of the XANES and EXAFS suggests the enriched metallic Pt^0 and oxidized Pt species over the Pt/p-CNF and Pt/f-CNF catalyst, respectively, which is well consistent with the XPS results.

To this point, it remains an open question whether and how these Pt-O-C linkages affect the catalytic performance. Considering the strong reducibility of ammonia borane, the Pt-O-C linkages could be unstable and in-situ reduced to metallic Pt^0 species by ammonia borane during the concomitant hydrolysis reaction. To investigate the stability of Pt-O-C linkages, the fresh Pt/f-CNF and Pt/p-CNF precursors without H_2 reduction were directly mixed with ammonia borane solution to catalyze the reaction. As shown in Figure 4d, both two catalysts exhibit the induction period at the beginning of reaction, ascribed to the reduction of Pt precursors and the concomitantly catalyzed hydrogen generation. Afterwards, there remains a liner relationship between hydrogen generation volume and reaction time. Similarly, the reaction rates (r) for these two catalysts could be calculated based on the slope of linear part for each plot as 107 and 139 $mol_{H2}{\cdot}mol_{Pt}^{-1}{\cdot}min^{-1}$, respectively (Table 3). Obviously, both two catalysts in situ reduced by AB

deliver less than one thirds of catalytic activity compared with their corresponding catalysts ex-situ reduced by H_2. After the completion of hydrogen generation, the two used catalysts were isolated from the spent reaction solution for further characterization and labelled as AB-Pt/f-CNF and AB-Pt/p-CNF, respectively.

Table 3 The percentage of Pt species and Pt^0 $4f_{7/2}$ binding energy determined by XPS, as well as reaction rate (r) of AB-Pt/f-CNF, AB-Pt/p-CNF, Ar-Pt/f-CNF and Ar-Pt/p-CNF.

Catalyst	Pt species content			Pt^0 $4f_{7/2}$	r
	Pt^0	Pt^{2+}	Pt^{4+}	B.E. (eV)	($mol_{H2}·mol_{Pt}^{-1}·min^{-1}$)
AB-Pt/f-CNF	53.7%	29.0%	17.3%	71.6	107
AB-Pt/p-CNF	66.0%	22.0%	11.9%	71.9	139
Ar-Pt/f-CNF	39.8%	31.7%	28.5%	71.9	68
Ar-Pt/p-CNF	51.9%	26.5%	21.6%	71.9	73

Along this line, HAADF-STEM was employed to characterize these two in-situ reduced catalysts. As shown in Figure S1, a slight increase of Pt particle size could be observed for these two AB-reduced catalysts compared with the corresponding H_2-reduced catalysts, which suggests that the gas-phase reduction by H_2 may benefit the diffusion of Pt atoms on the carbon surfaces and obtain dispersed Pt nanoparticles. However, the slight increase in Pt particle size is insufficient to explain the remarkably decreased catalytic activity, and thus it is tempting to attribute that to their electronic effects. Similarly, XPS was used to explore the Pt-carbon electronic interactions within the AB-reduced catalysts and the results are shown in Figure 5. The deconvolution

result as summarized in Table 3 reveals that compared with the H_2-reduced catalysts, AB-Pt/f-CNF and AB-Pt/p-CNF show significant downshifts in Pt binding energy of 0.4 and 0.2 eV, respectively, ascribed to the electron transfer from the electron-negative oxygen within the AB reduction product to Pt particles [45]. Accordingly, these AB-reduced catalysts with lower Pt binding energy exhibit much poorer catalytic activity, consistent with the above influence of Pt binding energy. Moreover, as shown in Table 3, it can be seen that the AB-reduced catalysts show similar percentages of metallic Pt^0 species as those of H_2-reduced catalysts, which account for 53.7% and 66.0% of the total Pt species, respectively. This indicates that the Pt-O-C linkages are too stable to be reduced by either H_2 or AB. Therefore, it is reasonable to deduce that the number of Pt-O-C linkages within Pt-carbon interfaces determined by XPS could reflect that in real reaction conditions, whose change during the reaction could be minimal.

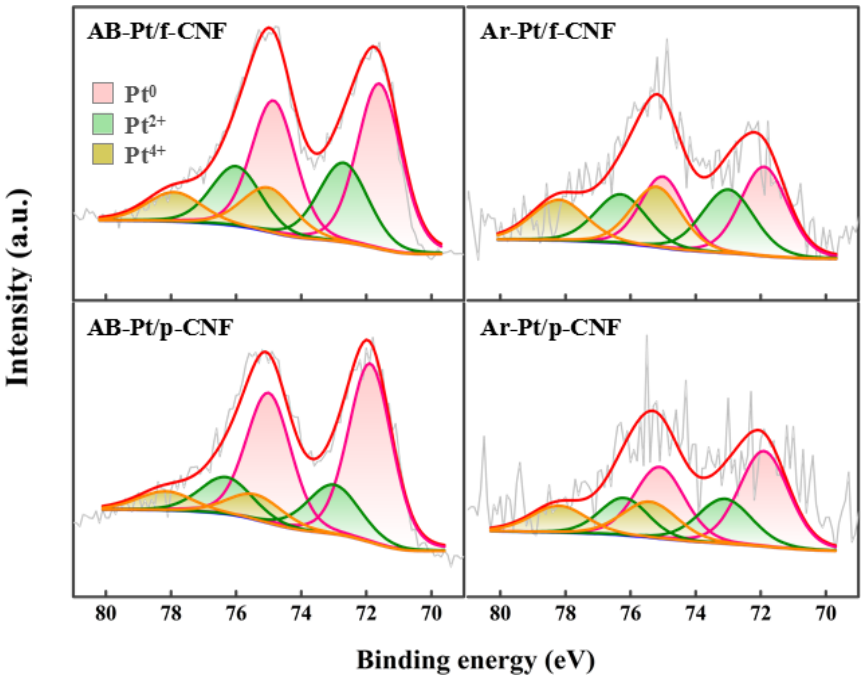

Figure 5. XPS Pt 4f spectra of AB-Pt/f-CNF, AB-Pt/p-CNF, Ar-Pt/f-CNF and Ar-Pt/p-CNF.

In light of the number of Pt-O-C linkages being almost unchanged during the reaction, we can separately investigate their catalytic properties from metallic Pt^0 species, and then correlate them with the overall catalytic activity. Herein, in order to introduce more Pt-O-C linkages, the two catalysts precursors were treated under Ar atmosphere instead of H_2 at the same temperature of 250 ^oC. The resultant Ar-treated catalysts are labelled as Ar-Pt/f-CNF and Ar-Pt/p-CNF, and their structural as well as electronic properties were characterized by HAADF-STEM and XPS, respectively. Figure S2 display the typical HAADF-STEM images of these two catalysts, which exhibit homogeneous distribution of Pt nanoparticles despite of a few agglomerations for each catalyst. On the other hand, the deconvolution of Pt 4f spectra in Figure 5 was conducted to probe Pt-carbon electronic interactions and the results are summarized in Table 3. It is obviously that, upon Ar treatment, the percentages of metallic Pt^0 for both two catalysts decrease sharply with respect to those reduced by either H_2 or AB, which is 39.8% and 51.9% for Ar-Pt/f-CNF and Ar-Pt/p-CNF, respectively. Because no oxygen was introduced into the catalysts during Ar treatment at 250 ^oC, the decrease of metallic Pt^0 species could originate from more Pt atoms interacting with the oxygen-containing groups on carbon surfaces upon Ar treatment, giving rise to more Pt-O-C linkages, especially for Ar-Pt/f-CNF with abundant surface oxygen-containing groups. Accordingly, these two Ar-treated Pt catalysts with more Pt-O-C linkages were tested for the hydrolytic dehydrogenation of ammonia borane at the same conditions. As shown in Figure 4d, both two catalysts show much lower hydrogen generation rate.

Based on the slope of the linear part for each plot, the reaction rate could be respectively calculated as 68 and 73 $mol_{H2} \cdot mol_{Pt}^{-1} \cdot min^{-1}$ for Ar-Pt/f-CNF and Ar-Pt/p-CNF, which is only one fifth of that for the corresponding catalyst reduced by H_2. Therefore, a combination of the characterization results and catalytic performance suggests that the oxidized Pt species within Pt-O-C linkages are highly stable yet much less active for this reaction. Hence, Pt/p-CNF with the highest Pt binding energy and least Pt-O-C linkages demonstrates the highest catalytic activity among all the catalysts.

4. Conclusions

In summary, we have systemically demonstrated how the Pt-carbon interactions can yield significant influences on the structural and electronic properties of Pt nanoparticles, as well as the resultant catalytic performances for hydrogen generation from AB. Four types of carbon materials (AC, CNT, f-CNF and p-CNF) have been adopted as the supports to immobilize similarly sized Pt nanoparticles, affording a 20-fold increase of hydrogen generation rate. A combination of HAADF-STEM, N_2 physisorption, XRD, Raman, TG, H_2-TPR, XPS and XAFS characterization has revealed that the electron transfer and interfacial bonding within the Pt-carbon interactions are mainly responsible for the remarkable enhancement in the catalytic activity. The surface-enriched electron-withdrawing groups on p-CNF surface are found to capture electrons from Pt, giving rise to the highest Pt binding energy, which vice versa for AC. As a result, n_{EWG}/n_{EDG} has been identified as a good descriptor of catalyst in terms of Pt binding energy, which exhibits an almost linear relationship with

the catalytic activity. Moreover, a comparison of Pt catalysts pre-treatments has revealed that the Pt-O-C linkages within the Pt-carbon interactions are highly stable yet inferior to this reaction. Therefore, combining the merits of the highest Pt binding energy with the least Pt-O-C linkages, Pt/p-CNF has delivered the highest catalytic activity among all the catalysts. The insights gained here could shed new lights on the design and preparation of highly efficient metal-carbon catalysts.

Acknowledgments

This work was financially supported by the Natural Science Foundation of China (21922803 and 21776077), the China Postdoctoral Science Foundation (BX20190116), the Program for Professor of Special Appointment (Eastern Scholar) at Shanghai Institutions of Higher Learning, the State Key Laboratory of Organic-Inorganic Composites (oic-201801007), 111 Project of the Ministry of Education of China (B08021) and the Open Project of State Key Laboratory of Chemical Engineering (SKLChe-15C03). We thank the BL14W1 XAFS beamline of Shanghai Synchrotron Radiation Facility (SSRF) for providing beamtime.

References

[1] A.T. Bell, The impact of nanoscience on heterogeneous catalysis. Science 299 (2003) 1688-1691.

[2] D. Astruc, F. Lu, J.R. Aranzaes, Nanoparticles as recyclable catalysts: the frontier between homogeneous and heterogeneous catalysis. Angew. Chem. Int. Ed. 44 (2005)

7852-7872.

[3] J.K. Norskov, T. Bligaard, A. Logadottir, S. Bahn, L.B. Hansen, M. Bollinger, H. Bengaard, B. Hammer, Z. Sljivancanin, M. Mavrikakis, Y. Xu, Universality in heterogeneous catalysis. J. Catal. 209 (2002) 275-278.

[4] M. Comotti, W.C. Li, B. Spliethoff, F. Schuth, Support effect in high activity gold catalysts for CO oxidation. J. Am. Chem. Soc. 128 (2006) 917-924.

[5] X.Y. Liu, A. Wang, T. Zhang, C.Y. Mou, Catalysis by gold: new insights into the support effect. Nano Today 8 (2013) 403-416.

[6] G.R. Jenness, J.R. Schmidt, Unraveling the role of metal-support interactions in heterogeneous catalysis: oxygenate selectivity in Fischer-Tropsch synthesis. ACS Catal. 3 (2013) 2881-2890.

[7] E.O. Pentsak, E.G. Gordeev, V.P. Ananikov, Noninnocent nature of carbon support in metal/carbon catalysts: etching/pitting vs nanotube growth under microwave irradiation. ACS Catal. 4 (2014) 3806-3814.

[8] M. Mao, H. Lv, Y. Li, Y. Yang, M. Zeng, N. Li, X. Zhao, Metal support interaction in Pt nanoparticles partially confined in the mesopores of microsized mesoporous CeO_2 for highly efficient purification of volatile organic compounds. ACS Catal. 6 (2015) 418-427.

[9] G.M. Schwab, Boundary-layer catalysis. Angew. Chem. Int. Ed. 6 (1967) 375-375.

[10] Y. Nagai, T. Hirabayashi, K. Dohmae, N. Takagi, T. Minami, H. Shinjoh, S.I. Matsumoto, Sintering inhibition mechanism of platinum supported on ceria-based oxide and Pt-oxide-support interaction. J. Catal. 242 (2006) 103-109.

[11] S. Altieri, L.H. Tjeng, G.A. Sawatzky, Electronic structure and chemical reactivity of oxide-metal interfaces: MgO (100)/Ag (100). Phys. Rev. B 61 (2000) 16948.

[12] G. Jacobs, T.K. Das, Y. Zhang, J. Li, G. Racoillet, B.H. Davis, Fischer-Tropsch synthesis: support, loading, and promoter effects on the reducibility of cobalt catalysts. Appl. Catal. A: Gen. 233 (2002) 263-281.

[13] J. Zhu, A. Holmen, D. Chen, Carbon nanomaterials in catalysis: proton affinity, chemical and electronic properties, and their catalytic consequences, ChemCatChem, 5 (2013) 378-401.

[14] P. Serp, M. Corrias, P. Kalck, Carbon nanotubes and nanofibers in catalysis, Appl. Catal. A: Gen. 253 (2003) 337-358.

[15] D.S. Su, R. Schlogl, Nanostructured carbon and carbon nanocomposites for electrochemical energy storage applications, ChemSusChem 3 (2010) 136-168.

[16] B.F. Machado, P. Serp, Graphene-based materials for catalysis. Catal. Sci. Tech. 2 (2012) 54-75.

[17] X. Fan, G. Zhang, F. Zhang, Multiple roles of graphene in heterogeneous catalysis. Chem. Soc. Rev. 44 (2015) 3023-3035.

[18] D.H. Lim, J. Wilcox, DFT-based study on oxygen adsorption on defective graphene-supported Pt nanoparticles. J. Phys. Chem. C 115 (2011) 22742-22747.

[19] D.H. Lim, A.S. Negreira, J. Wilcox, DFT Studies on the interaction of defective graphene-supported Fe and Al nanoparticles. J. Phys. Chem. C 115 (2011) 8961-8970.

[20] Y. Li, Y. Yu, J.G. Wang, J. Song, Q. Li, M. Dong, C.J. Liu, CO oxidation over graphene supported palladium catalyst. Appl. Catal. B: Environ. 125 (2012) 189-196.

[21] R.G. Rao, R. Blume, T.W. Hansen, E. Fuentes, K. Dreyer, S. Moldovan, O. Ersen, D.D. Hibbitts, Y.J. Chabal, R. Schlogl, J.P. Tessonnier, Interfacial charge distributions in carbon-supported palladium catalysts. Nat. Commun. 8 (2017) 340.

[22] W. Zhu, Z. Wu, G.S. Foo, X. Gao, M. Zhou, B. Liu, G.M. Veith, P. Wu, K.L. Browning, H.N. Lee, H. Li, Taming interfacial electronic properties of platinum nanoparticles on vacancy-abundant boron nitride nanosheets for enhanced catalysis. Nat. Commun. 8 (2017) 15291.

[23] M.L. Toebes, F.F. Prinsloo, J.H. Bitter, A.J. van Dillen, K.P. de Jong, Influence of oxygen-containing surface groups on the activity and selectivity of carbon nanofiber-supported ruthenium catalysts in the hydrogenation of cinnamaldehyde. J. Catal. 214 (2003) 78-87.

[24] H.R. Byon, B.M. Gallant, S.W. Lee, S.H. Yang, Role of oxygen functional groups in carbon nanotube/graphene freestanding electrodes for high performance lithium batteries. Adv. Funct. Mater. 23 (2013) 1037-1045.

[25] W.Y. Chen, J. Ji, X.Z. Duan, G. Qian, P. Li, X.G. Zhou, D. Chen, W.K. Yuan, Unique reactivity in Pt/CNT catalyzed hydrolytic dehydrogenation of ammonia borane, Chem. Commun. 50 (2014) 2142-2144.

[26] W.Y. Chen, X.Z. Duan, G. Qian, D. Chen, X.G. Zhou, Carbon nanotubes as support in the platinum-catalyzed hydrolytic dehydrogenation of ammonia borane. ChemSusChem 8 (2015) 2927-2931.

[27] A. Aijaz, A. Karkamkar, Y.J. Choi, N. Tsumori, E. Ronnebro, T. Autrey, H. Shioyama, Q. Xu, Immobilizing highly catalytically active Pt nanoparticles inside the

pores of metal–organic framework: a double solvents approach. J. Am. Chem. Soc. 134 (2012) 13926-13929.

[28] X. Wang, D. Liu, S. Song, H. Zhang, Synthesis of highly active Pt-CeO_2 hybrids with tunable secondary nanostructures for the catalytic hydrolysis of ammonia borane. Chem. Commun. 48 (2012) 10207-10209.

[29] M.A. Khalily, H. Eren, S. Akbayrak, H.H. Susapto, N. Biyikli, S. Ozkar, M.O. Guler, Facile synthesis of three-dimensional Pt-TiO_2 Nano-networks: A highly active catalyst for the hydrolytic dehydrogenation of ammonia-borane. Angew. Chem. Int. Ed. 55 (2016) 12257-12261.

[30] X. Ning, Y. Li, B. Dong, H. Wang, H. Yu, F. Peng, Y. Yang, Electron transfer dependent catalysis of Pt on N-doped carbon nanotubes: effects of synthesis method on metal-support interaction. J. Catal. 348 (2017) 100-109.

[31] J.K. Zhang, C.Q. Chen, S. Chen, Q.M. Hu, Z. Gao, Y.Q. Li, Y. Qin, Highly dispersed Pt nanoparticles supported on carbon nanotubes produced by atomic layer deposition for hydrogen generation from hydrolysis of ammonia borane. Catal. Sci. Technol. 7 (2017) 322-329.

[32] C.F. Yao, L. Zhuang, Y.L. Cao, X.P. Ai, H.X. Yang, Hydrogen release from hydrolysis of borazane on Pt-and Ni-based alloy catalysts. Int. J. Hyd. Energy 33 (2008) 2462-2467.

[33] E.L. Kunkes, D.A. Simonetti, J.A. Dumesic, W.D. Pyrz, L.E. Murillo, J.G. Chen, D.J. Buttrey, The role of rhenium in the conversion of glycerol to synthesis gas over carbon supported platinum-rhenium catalysts. J. Catal. 260 (2008) 164-177.

[34] B.M. Wyvratt, J.R. Gaudet, Thompson, L.T., Effects of passivation on synthesis, structure and composition of molybdenum carbide supported platinum water–gas shift catalysts. J. Catal. 330 (2015) 280-287.

[35] T. Ressler, WinXAS: a program for X-ray absorption spectroscopy data analysis under MS-Windows. J. Synchrotron Radiat. 5 (1998) 118-122.

[36] A.L. Ankudinov, B. Ravel, J.J. Rehr, S.D. Conradson, Real-space multiple-scattering calculation and interpretation of X-ray-absorption near-edge structure. Phys. Rev. B, 58 (1998) 7565-7576.

[37] W.Y. Chen, J. Ji, X. Feng, X.Z. Duan, G. Qian, P. Li, X.G. Zhou, D. Chen, W.K. Yuan, Mechanistic insight into size-dependent activity and durability in Pt/CNT catalyzed hydrolytic dehydrogenation of ammonia borane, J. Am. Chem. Soc. 136 (2014) 16736-16739.

[38] A. Sadezky, H. Muckenhuber, H. Grothe, R. Niessner, U. Poschl, Raman microspectroscopy of soot and related carbonaceous materials: spectral analysis and structural information, Carbon 43 (2005) 1731-1742.

[39] T.G. Ros, A.J. Van Dillen, J.W. Geus, D.C. Koningsberger, Surface oxidation of carbon nanofibres. Chem. Eur. J. 8 (2002) 1151-1162.

[40] M.L. Toebes, J.M. van Heeswijk, J.H. Bitter, A.J. Van Dillen, K.P. de Jong, The influence of oxidation on the texture and the number of oxygen-containing surface groups of carbon nanofibers. Carbon 42 (2004) 307-315.

[41] J.H. Zhou, Z.J. Sui, J. Zhu, P. Li, D. Chen, Y.C. Dai, W.K. Yuan, Characterization of surface oxygen complexes on carbon nanofibers by TPD, XPS and FT-IR. Carbon

45 (2007) 785-796.

[42] N.G. Akalework, C.J. Pan, W.N. Su, J. Rick, M.C. Tsai, J.F. Lee, J.M. Lin, L.D. Tsai, B.J. Hwang, Ultrathin TiO_2-coated MWCNTs with excellent conductivity and SMSI nature as Pt catalyst support for oxygen reduction reaction in PEMFCs. J. Mater. Chem. 22 (2012) 20977-20985.

[43] Z.Z. Jiang, Z.B. Wang, D.M. Gu, E.S. Smotkin, Carbon riveted Pt/C catalyst with high stability prepared by in situ carbonized glucose. Chem. Commun. 46 (2010) 6998-7000.

[44] J.R. Croy, S. Mostafa, H. Heinrich, B.R. Cuenya, Size-selected Pt nanoparticles synthesized via micelle encapsulation: effect of pretreatment and oxidation state on the activity for methanol decomposition and o1xidation. Catal. Lett. 131 (2009) 21-32.

[45] W.Y. Chen, Z.J. Wang, X.Z. Duan, G. Qian, D. Chen, X.G. Zhou, Structural and kinetic insights into Pt/CNT catalysts during hydrogen generation from ammonia borane. Chem. Eng. Sci. 192 (2018) 1242-1251.